Linköping University Post Print

Cubic $Sc_{1-x}Al_xN$ solid solution thin films deposited by reactive magnetron sputter epitaxy onto ScN(111)

Carina Höglund, Javier Bareno, Jens Birch, Björn Alling, Zsolt Czigany and Lars Hultman

N.B.: When citing this work, cite the original article.

Original Publication:

Carina Höglund, Javier Bareno, Jens Birch, Björn Alling, Zsolt Czigany and Lars Hultman, Cubic $Sc_{1-x}Al_xN$ solid solution thin films deposited by reactive magnetron sputter epitaxy onto ScN(111), 2009, JOURNAL OF APPLIED PHYSICS, (105), 11, 132862.
http://dx.doi.org/10.1063/1.3132862

Copyright: American Institute of Physics
http://www.aip.org/

Postprint available at: Linköping University Electronic Press
http://urn.kb.se/resolve?urn=urn:nbn:se:liu:diva-19664

Cubic $Sc_{1-x}Al_xN$ solid solution thin films deposited by reactive magnetron sputter epitaxy onto ScN(111)

Carina Höglund,[1,a)] Javier Bareño,[1] Jens Birch,[1] Björn Alling,[2] Zsolt Czigány,[3] and Lars Hultman[1]

[1]*Department of Physics, Chemistry and Biology (IFM), Thin Film Physics Division, Linköping University, S-581 83 Linköping, Sweden*

[2]*Department of Physics, Chemistry and Biology (IFM), Theory and Modeling Division, Linköping University, S-581 83 Linköping, Sweden*

[3]*Research Institute for Technical Physics and Materials Science, Hungarian Academy of Sciences, P.O. Box 49, H-1525 Budapest, Hungary*

(Received 24 February 2009; accepted 18 April 2009; published online 5 June 2009)

Reactive magnetron sputter epitaxy was used to deposit thin solid films of $Sc_{1-x}Al_xN$ $(0 \leq x \leq 1)$ onto MgO(111) substrates with ScN(111) seed layers. Stoichiometric films were deposited from elemental Sc and Al targets at substrate temperatures of 600 °C. The films were analyzed by Rutherford backscattering spectroscopy, elastic recoil detection analysis, x-ray diffraction, and transmission electron microscopy. Results show that rocksalt structure (c)-$Sc_{1-x}Al_xN$ solid solutions with AlN molar fractions up to ~60% can be synthesized. For higher AlN contents, the system phase separates into c- and wurtzite structure (w)-$Sc_{1-x}Al_xN$ domains. The w-domains are present in three different orientations relative to the seed layer, namely, $Sc_{1-x}Al_xN(0001) \parallel ScN(111)$ with $Sc_{1-x}Al_xN[\bar{1}2\bar{1}0] \parallel ScN[1\bar{1}0]$, $Sc_{1-x}Al_xN(10\bar{1}1) \parallel ScN(111)$ with $Sc_{1-x}Al_xN[\bar{1}2\bar{1}0] \parallel ScN[1\bar{1}0]$, and $Sc_{1-x}Al_xN(10\bar{1}1) \parallel ScN(113)$. The results are compared to first-principles density functional theory calculations for the mixing enthalpies of c-, w-, and zinc blende $Sc_{0.50}Al_{0.50}N$ solid solutions, yielding metastability with respect to phase separation for all temperatures below the melting points of AlN and ScN. © *2009 American Institute of Physics*. [DOI: 10.1063/1.3132862]

I. INTRODUCTION

Pseudobinary alloys, which are solid solutions of two binary compounds with one common element, typically allow tuning of electrical and structural properties in the range between the end components. Successful examples of this approach include band gap engineering and lattice matching in zinc blende structure (zb) $Ga_{1-x}In_xAs$,[1] wurtzite structure (w) group III nitrides,[2] and more recently in rocksalt structure (c) nitrides. As an example, ScN is combined with wide band gap semiconductor GaN mainly due to the small lattice mismatch of <2% between ScN and GaN, intended for optoelectronic devices.[3–5] Transition metal (TM) nitrides, e.g., TiN and CrN, form rocksalt structure solid solutions with AlN in $TM_{1-x}Al_xN$ and are extensively used to increase the lifetime and cutting speed of coated tools.[6–8]

Here, we consider the solid solutions of c-ScN and c-AlN in $Sc_{1-x}Al_xN$, where Sc and Al are positioned on the metal sublattice and $0 \leq x \leq 1$. The Sc–Al–N material system is, in comparison to the related systems mentioned, almost unexplored, with the perovskite Sc_3AlN as the only reported ternary phase[9] and a brief report about an enhanced piezoelectric response in hexagonal $Sc_{1-x}Al_xN$.[10]

Group IIIA semiconducting w-AlN, with physical properties including wide energy band gap (6.2 eV),[11] high hardness (>20 GPa),[12,13] high thermal conductivity (3.19 W/cm K at RT),[14] and high-temperature stability (melting point of >2000 °C),[15] has been extensively studied mainly for optical and electronic device applications. The metastable cubic AlN polytypes (c and zb) are less explored due to the difficulties to synthesize them in a pure form. The lattice parameter is, though, experimentally measured to be 4.05 Å (Ref. 16) for c-AlN and calculations estimate an indirect band gap of ~5.0 eV.[17] This form of AlN is mainly considered as a part in forming the $TM_{1-x}Al_xN$ solid solutions mentioned above.

The semiconducting group IIIB nitride c-ScN also has exceptional properties, such as a hardness of 21 GPa (Ref. 18) and a high-temperature stability with a melting temperature of 2600 °C.[19] Calculations estimate the indirect band gap to be 0.9–1.6 eV (Refs. 20–23) and the lattice parameter to be 4.521 Å,[24] while experimentally the lattice parameter is measured to be 4.50 Å.[25] Its thermodynamically stable crystal structure is rocksalt, even though it is also predicted to form a metastable hexagonal phase.[26] c-ScN is still relatively little explored. Most reports are theoretical predictions of various properties including a long debate on whether ScN is a semimetal or semiconductor, with the latest reports determining that the material is semiconducting.[20–23] Experimentally the synthesis of c-ScN as thin films is reported with different techniques including reactive magnetron sputter epitaxy (MSE),[27] radio frequency molecular beam epitaxy,[28] and chemical vapor deposition.[29] Moram *et al.*[30] showed that ScN has a high affinity to oxygen compared to other TM nitrides. High amounts of impurities are probably the reason for the variation in the experimentally measured properties and their variation from theoretical predictions.

$Sc_{1-x}Al_xN$ pseudobinary alloys are expected to have ex-

a)Electronic mail: carina@ifm.liu.se.

 © 2009 American Institute of Physics

Downloaded 04 Nov 2009 to 130.236.83.91. Redistribution subject to AIP license or copyright; see http://jap.aip.org/jap/copyright.jsp

cellent mechanical properties due to the similarities with the related hard-to-superhard $TM_{1-x}Al_xN$ materials. The difference in lattice parameter between c-ScN (Ref. 25) and c-AlN (Ref. 16) is almost −10%, while the difference in band gap is 3.4–4.1 eV.[17,21,23] This large difference in both volume and electronic structure gives the possibility to design materials with a wide range of both lattice parameters and band gaps. Recently Alling *et al.*[24] reported of first-principles calculations on the mixing enthalpies, lattice parameters, and electronic density of states of c-$Sc_{1-x}Al_xN$. There are, however, to the best of our knowledge, no reports on the synthesis of such solid solutions.

This paper concentrates on thin film deposition and characterization of $Sc_{1-x}Al_xN$ starting from optimal conditions for pure ScN, followed by an increase in Al molar fraction reaching pure AlN. The epitaxial films were deposited by MSE onto MgO(111) substrates capped with a ScN(111) seed layer. ScN was successfully alloyed with AlN molar fractions up to ~60%, while retaining the rocksalt structure. Higher AlN contents yielded wurtzite structured films presenting two new epitaxial relationships between the film and the c-ScN seed layers.

II. EXPERIMENTAL PROCEDURES

Deposition experiments were performed in an ultrahigh-vacuum chamber at a base pressure of 1.33×10^{-6} Pa. MSE using unbalanced type II magnetrons with 50 mm diameter Sc and 75 mm diameter Al elemental targets was used to grow 55 nm thick ScN(111) seed layers onto polished $10\times10\times0.5$ mm^3 MgO(111) substrates, followed by 50–60 nm thick films of $Sc_{1-x}Al_xN$, with x reaching from 0 to 1. The MSE system is described in detail elsewhere.[31]

The ScN(111) seed layers were chosen because they are temperature stable, constitute good diffusion barriers, and are good templates for the films, especially for the ones with lowest AlN content. MgO(111) substrates were chosen as the base substrate due to their temperature stability and the fact that they provide a good lattice match to the ScN seed layers (in-plane lattice mismatch of +6.7%). Considered alternative substrates with a good enough temperature stability were $MgAl_2O_4(111)$ and $Al_2O_3(0001)$. Due to their higher lattice mismatch to ScN(111) (of +11.2% and +15.6%, respectively), these substrates yielded worse crystalline quality ScN(111) seed layers compared to MgO(111). In this work, $MgAl_2O_4(111)$ substrates were used as an alternative for those molar fractions x, where the film peaks in x-ray diffraction (XRD) would overlap with the ones from MgO(111).

Prior to deposition, the substrates were cleaned in ultrasonic baths of trichloroethylene, acetone, and 2-propanol and blown dry in dry N_2. This was followed by degassing in the vacuum chamber at 900 °C for 1 h before ramping down to the deposition temperature of 600 °C, controlled by a thermocouple positioned behind the substrate and calibrated by pyrometry. During deposition, the N_2 and Ar partial pressures were kept at 0.13 and 1.07 Pa, respectively. The substrate potential was set to be floating.

The magnetron power for the ScN seed layers was set to 200 W. For the $Sc_{1-x}Al_xN$ layers, the Sc magnetron powers were 200, 180, 140, 100, 60, 20, or 0 W for seven different depositions, while the Al magnetron powers were adjusted accordingly to keep a total power of 200 W. This yielded a deposition rate of approximately 0.9 Å/s. Rutherford backscattering spectroscopy (RBS) results show that the molar fractions x vary linearly with the Al and Sc magnetron powers.

The film composition was determined by RBS using a 2 MeV He^+ beam at 60° incidence and 172° scattering angle. Elastic recoil detection analysis (ERDA), using a 40 MeV $^{127}I^{9+}$ beam at 67.5° incidence and 45° scattering angle and evaluated with the CONTES code,[32] was used to check for impurities in the films. The crystal structure was characterized by Cu $K\alpha$ XRD using a Philips Bragg–Brentano diffractometer. Cross-sectional transmission electron microscopy (XTEM) was carried out with an FEI Tecnai G2 TF 20 UT FEG microscope operated at 200 kV.

In parallel, first-principles calculations for mixing enthalpies of c-, w-, and zb-$Sc_{0.50}Al_{0.50}N$ solid solutions were carried out within a density functional theory framework. The projector augmented wave method as implemented in the Vienna *ab initio* simulation package[33–35] was used together with the generalized gradient approximation (GGA) (Ref. 36) for the exchange-correlation functional. The nitrogen sublattice was considered to be fully stoichiometric. The metal sublattice was modeled as a random alloy with the quasirandom structure model, which was first suggested by Zunger *et al.*[37] and is further described in Refs. 24 and 38.

III. RESULTS AND DISCUSSION

Compositional analysis was performed with both RBS and ERDA. RBS shows that the films and ScN seed layers are stoichiometric to within ±5 at.%. The Al to Sc molar ratios in the films are 0/100, 14/86, 29/71, 51/49, 73/27, 90/10, and 100/0 (corresponding to AlN molar fractions of x =0, 0.14, 0.29, 0.51, 0.73, 0.90, and 1.00). Two typical spectra together with fitting curves are shown in Figs. 1(a) and 1(b) for $Sc_{0.86}Al_{0.14}N$ and $Sc_{0.49}Al_{0.51}N$ films, respectively. In both spectra, the contribution from Sc in the seed layers can clearly be separated from Sc in the films. The sharp edges of all peaks show that there has been no interdiffusion between substrates, seed layers, and films. With this technique, the N content can only be estimated by subtracting atomic percentages of Sc and Al from 100% because of the overlap in RBS spectra between the MgO substrate and N in the film and seed layers; i.e., one needs to assume that no other light elements are incorporated. The O content is relatively high throughout the whole depth in $Sc_{0.86}Al_{0.14}N$ and on the surface of $Sc_{0.49}Al_{0.51}N$ but is better quantified with ERDA (see below). The RBS spectrum from $Sc_{0.49}Al_{0.51}N$, in Fig. 1(b), shows that the sputter rate from a 50 mm diameter Sc target and a 75 mm diameter Al target is almost the same under the mentioned conditions.

ERDA depth profiling was used to confirm the 50 at. % N content of the films estimated by RBS. The compositional ratios between Sc and Al were found to agree with the ones determined by RBS to within 2–3 at. %. The resolution of

Downloaded 04 Nov 2009 to 130.236.83.91. Redistribution subject to AIP license or copyright; see http://jap.aip.org/jap/copyright.jsp

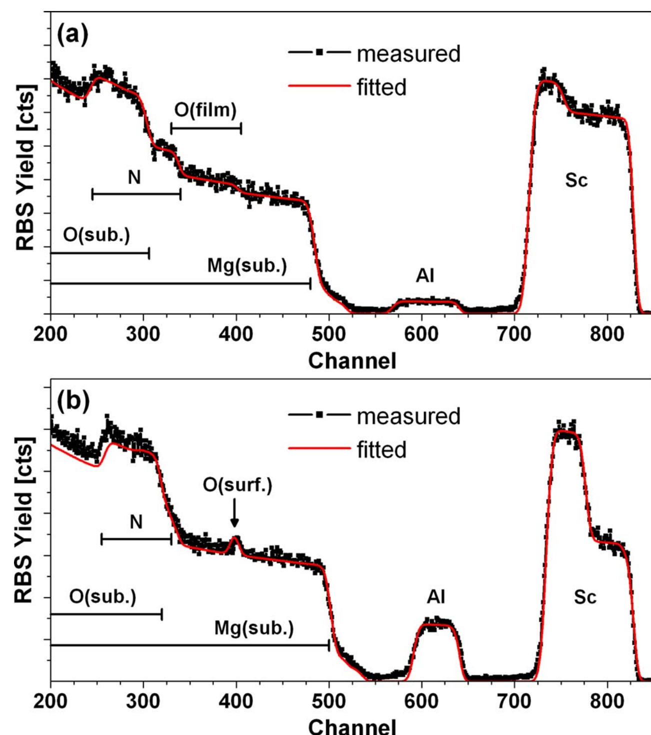

FIG. 1. (Color online) RBS spectra at 60° incoming angle from (a) a $Sc_{0.86}Al_{0.14}N$ film and (b) a $Sc_{0.49}Al_{0.51}N$ film grown on MgO(111) substrates with ScN(111) seed layers.

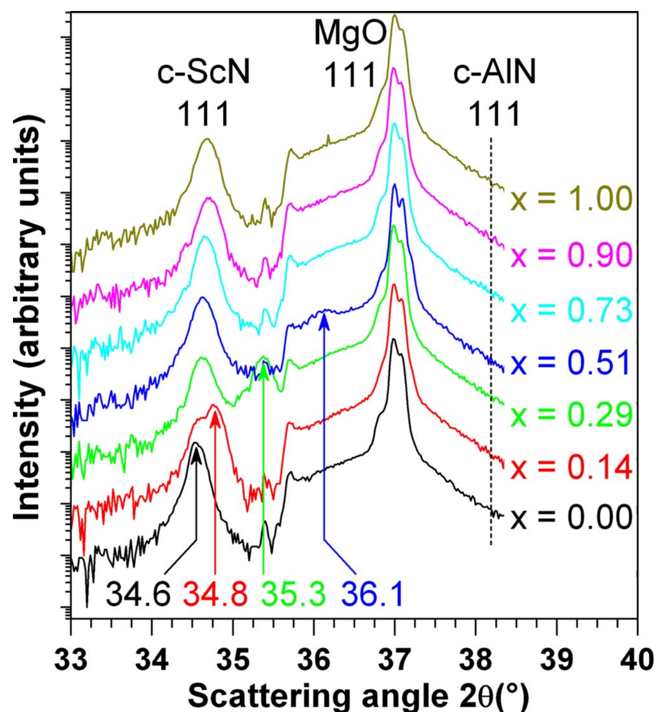

FIG. 3. (Color online) XRD data from $Sc_{1-x}Al_xN(111)$ films on MgO(111) substrates and ScN(111) seed layers with different Al fractions, x, from 0 to 1 in seven steps. The additional peaks at $2\theta=35.4°$ originate from W $L\alpha$ x-rays diffracted on MgO 111.

the ERDA depth profiles is limited by the film thickness employed of only ~50 nm. The N content is nevertheless found to be close to 50 at. % and constant through the whole depth for all samples with AlN molar fractions larger than $x=0.14$. Figure 2(a) shows the depth profile from a sample with $x=0.51$ including the MgO substrate and the ScN seed layer. It can be seen that this film contains ~25 at. % of both Sc and Al, and that the N content is ~47 at. %. A high amount of oxygen on the surface, however, lowers the Sc, Al, and N profiles proportionally from their expected values, which was also seen in the RBS spectra in Fig. 1(b). Depth profiles of samples with the lowest amount of Al ($x=0$ and $x=0.14$) show that these samples contain more than 10 at. % O throughout the seed layers and films, as can be seen in Fig. 2(b) presenting a depth profile from a film with $x=0.14$. O has most likely diffused into the films along grain boundaries after the sample was taken out of the deposition chamber (cf. XTEM below). This statement is based on that all films and seed layers are grown under the same conditions and therefore are expected to be comparable. If O is incorporated during growth of Sc-rich films, it should be seen in the depth profile of the seed layers from all samples, which is not the case. It seems that a higher Al content increases the film density and hinders O diffusion into the film. As mentioned in Ref. 30, the affinity of O to ScN is high in comparison to other TM nitrides, which is supported by these observations. Also, the films with high amounts of O exhibit a significantly higher concentration of C and H impurities, which supports the idea of postgrowth indiffusion along grain boundaries under atmospheric conditions. Correspondingly, the C and H contents of all oxygen-free samples are close to the detection limits of ~0.1 at. % in ERDA. Furthermore, virtually all films contain ~0.1 at. % Ta, which is a common contaminant in Sc.

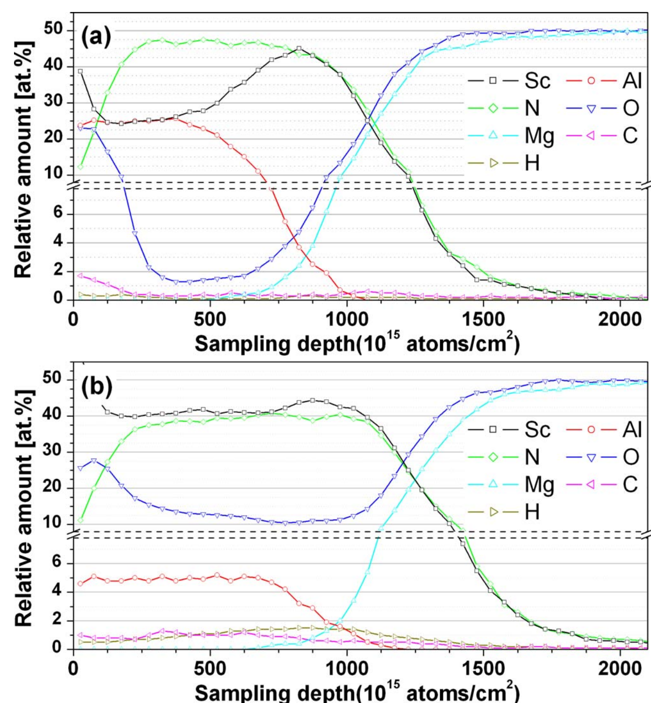

FIG. 2. (Color online) ERDA depth profiles from (a) a $Sc_{0.49}Al_{0.51}N$ film and (b) a $Sc_{0.86}Al_{0.14}N$ film grown on MgO(111) substrates with ScN(111) seed layers.

Figure 3 shows XRD data obtained from $Sc_{1-x}Al_xN$ samples with compositions x ranging from 0 to 1 on

Downloaded 04 Nov 2009 to 130.236.83.91. Redistribution subject to AIP license or copyright; see http://jap.aip.org/jap/copyright.jsp

ScN(111) and MgO(111). Both MgO 111 substrate and ScN 111 seed layer peaks are present in all samples with comparable full widths at half maximum. Replacing 14% of the Sc by Al ($x=0.14$) yields an extra peak at a scattering angle of 34.8°, corresponding to a cubic lattice parameter of 4.46 Å. Also for $x=0.29$ and $x=0.51$, additional peaks show up at angles corresponding to lattice parameters of 4.40 and 4.30 Å, respectively. The cubic type of the phases was proven with pole figures (not shown) and selected area electron diffraction (SAED) (presented below). For higher AlN contents, any film peak in the XRD pattern severely overlaps with the MgO 111 substrate peak and thus cannot be revealed. However, for a sample with $x=0.73$ grown on a $MgAl_2O_4(111)$ substrate, which has a smaller lattice parameter than MgO and therefore does not exhibit peak overlap, we obtained an XRD peak at an angle of 36.6° corresponding to a cubic lattice parameter of 4.25 Å. When following Vegard's rule[39] rocksalt structure films with $x=0.73$ are expected to have a lattice parameter of ~4.18 Å, while for the lattice parameter to be 4.25 Å, x is expected to be ~0.60. This leads us to suspect that this film consists of both c-$Sc_{0.40}Al_{0.60}N$ and at least one more phase. This additional phase is probably w-AlN or AlN-rich w-ScAlN due to the residuals of Al and N for an overall composition of $Sc_{0.27}Al_{0.73}N$. The larger in-plane lattice mismatch of ScN to the $MgAl_2O_4$ substrate unfortunately gives a worse template for a high quality seed layer and therefore inadequate conditions for epitaxial $Sc_{1-x}Al_xN$ film growth. In Fig. 3 it is also seen that samples with x larger than 0.90 do not show any additional peaks in XRD. This is probably due to both substrate peak overlaps and the expected small, few nanometers, size of the crystallites.

XTEM images with corresponding SAED patterns were recorded from three samples along the $[1\bar{1}0]$ zone axis of the substrate. Figures 4(a) and 4(b) show our results from a sample with $x=0.51$, the highest AlN content, for which only one c-$Sc_{1-x}Al_xN$ phase is seen in XRD. Figures 4(c) and 4(d) show images from a sample with $x=0.73$, which seems to be a mixture of c-$Sc_{1-x}Al_xN$ and another phase. Finally, in Figs. 4(e) and 4(f), images from a sample with high AlN content ($x=0.90$) are shown, for which no information was received from XRD measurements.

The overview XTEM image of a sample with $x=0.51$ in Fig. 4(a) shows the MgO substrate, the ScN seed layer, and the film. Both seed layer and film have a columnar structure, with the columns perpendicular to the substrate, but with no distinguishable interface in between. The film top surface is flat and without facets. The corresponding SAED pattern in Fig. 4(b) includes diffraction spots from MgO, ScN, and c-$Sc_{0.49}Al_{0.51}N$, situated very close to each other and highlighted in gray squares. The inset in Fig. 4(b) shows an enlarged view of the 002 reflections, where the one closest to the center comes from ScN, the second closest from $Sc_{0.49}Al_{0.51}N$, and the outermost from MgO. The order of the reflections and the relative distances between them are as expected from the lattice parameters calculated from XRD. This yields a cube-on-cube epitaxial relationship between $Sc_{0.49}Al_{0.51}N$, ScN, and MgO, with $Sc_{0.49}Al_{0.51}N(111)\|$ ScN(111)$\|$MgO(111) and $Sc_{0.49}Al_{0.51}N[1\bar{1}0]\|ScN[1\bar{1}0]\|$ MgO$[1\bar{1}0]$. When comparing this SAED pattern with the corresponding one from a sample with less AlN, it can also be seen that film reflections move closer to substrate reflections when increasing the AlN content. This is consistent with the decrease in lattice parameter with increasing AlN content, observed by XRD (cf. Fig. 3).

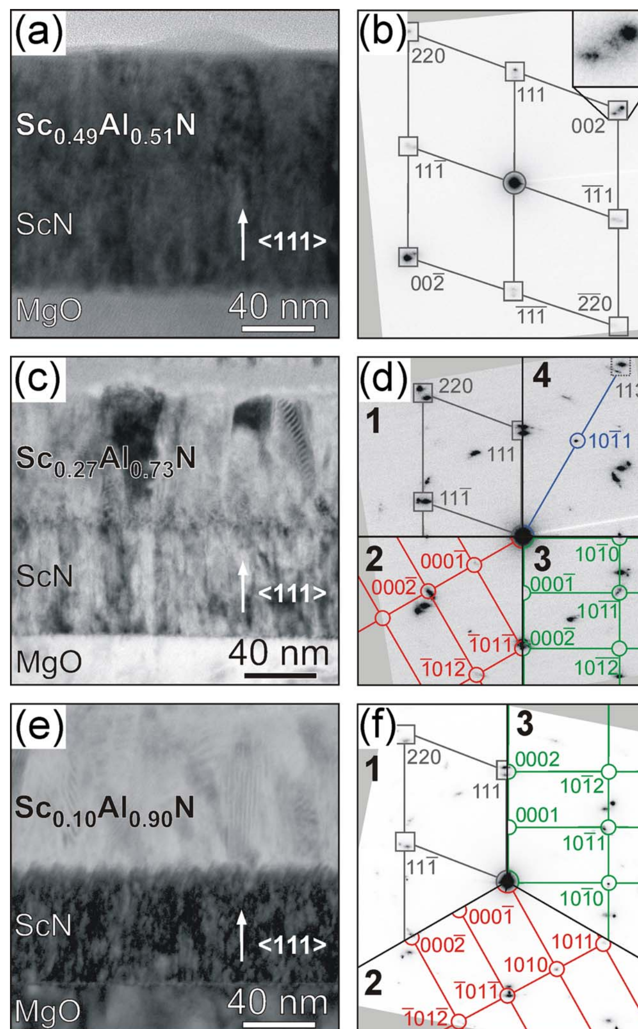

FIG. 4. (Color online) XTEM overview images (left) and corresponding inverted-contrast SAED patterns (right) from $Sc_{1-x}Al_xN$ films deposited onto MgO(111) substrates and ScN(111) seed layers, with $x=0.51$ in (a) and (b), $x=0.73$ in (c) and (d), and $x=0.90$ in (e) and (f). The growth direction ⟨111⟩ is indicated in the XTEM figures. The indexed SAED patterns along the $[1\bar{1}0]$ zone axis are mirrored and rotated to be comparable. Gray squares mark cubic reflections from substrate, seed layer and film in (b) [also seen in (d)(1) and (f)(1)]. The circles mark wurtzite structure (w) film reflections. In (d)(2) and (f)(2) the epitaxial relationship w-$Sc_{1-x}Al_xN(10\bar{1}1)\|ScN(111)$ is highlighted in red, in (d)(3) and (f)(3) w-$Sc_{1-x}Al_xN(0001)\|ScN(111)$ is highlighted in green, and in (d)(4) w-$Sc_{1-x}Al_xN(10\bar{1}0)\|ScN(113)$ is highlighted in blue. Enlarged in (b) are three 002 reflections, showing the cube-on-cube epitaxy of $Sc_{0.49}Al_{0.51}N$ to ScN and MgO.

The XTEM overview image of an $x=0.73$ sample in Fig. 4(c) reveals that the film structure is less columnar compared to the $x=0.51$ sample, suggestive of competitive growth of different crystallite orientations. There is a clear interface between the film and the seed layer. The SAED pattern from a sample with $x=0.73$, shown in Fig. 4(d), differs from the

Downloaded 04 Nov 2009 to 130.236.83.91. Redistribution subject to AIP license or copyright; see http://jap.aip.org/jap/copyright.jsp

pattern coming from the $Sc_{0.49}Al_{0.51}N$ film in Fig. 4(b) in that it contains four different film contributions, of which three correspond to a wurtzite structured film. The four relationships are indicated in Fig. 4(d), with reflections highlighted in the respective quadrants for

(1) cube-on-cube epitaxial contribution,
(2) growth of film $(10\bar{1}1)\parallel$ScN(111) and film $[\bar{1}2\bar{1}0]\parallel$ ScN$[1\bar{1}0]$,
(3) growth of film $(0001)\parallel$ScN(111) and film $[\bar{1}2\bar{1}0]\parallel$ ScN$[1\bar{1}0]$, and
(4) growth of film $(10\bar{1}1)\parallel$ScN(113), without an unambiguous crystallite orientation.

The diffraction patterns highlighted in quadrants (2)–(4) originate from a wurtzite structured phase, having the same lattice parameter as *w*-AlN. The four kinds of growth open for the possibility that not all domains have the same composition as the overall film composition. Therefore, the phases are referred to as *c*- or *w*-$Sc_{1-x}Al_xN$, with a total film composition of 73% AlN and 27% ScN.

The cubic contribution to the diffraction pattern from the $x=0.73$ film in Fig. 4(d) is highlighted in gray squares in the first quadrant of the pattern, with each square including substrate, seed layer, and eventually, parts of the film. The film and MgO substrate reflections overlap due to the similar lattice parameter at high AlN contents. Similar to the $x=0.51$ film, there is an indication for cube-on-cube epitaxy of the film to the seed layer from the broadening in the vicinity of the substrate reflections when comparing to (not shown) diffraction patterns from exclusively MgO. The observed broadening is in agreement with the peaks seen with XRD coming from the same film on a $MgAl_2O_4(111)$ substrate.

The first hexagonal-to-cubic epitaxial relationship between film and seed layer is seen in the second quadrant of the diffraction pattern in Fig. 4(d). It is highlighted in red and originates from a tilted basal plane growth. In Fig. 5(a) a schematic of such a growth along the zone axis is shown, and in Fig. 5(b) a top view of the interface is shown. It reveals an original epitaxial relationship of *w*-$Sc_{1-x}Al_xN(10\bar{1}1)\parallel$ScN(111) and *w*-$Sc_{1-x}Al_xN[\bar{1}2\bar{1}0]\parallel$ ScN$[1\bar{1}0]$ with an in-plane lattice mismatch of 1.95% along this direction. Along the perpendicular in-plane direction, the lattice mismatch is 2.19%.

Highlighted in green in the third quadrant is the part of the diffraction pattern coming from the basal plane growth of *w*-$Sc_{1-x}Al_xN$ onto ScN (111), in the epitaxial relationship *w*-$Sc_{1-x}Al_xN(0001)\parallel$ScN(111) and *w*-$Sc_{1-x}Al_xN[\bar{1}2\bar{1}0]\parallel$ ScN$[1\bar{1}0]$. In Fig. 5(c) the epitaxial relationship of this wurtzite structure film to the 111 surface of ScN is illustrated along the zone axis and in Fig. 5(d) a top view of the same is shown. This epitaxial relationship yields an in-plane lattice mismatch between *w*-$Sc_{1-x}Al_xN$ and the *c*-ScN seed layer of −2.25%.

The last contribution to the diffraction pattern that comes from *w*-$Sc_{1-x}Al_xN$ is highlighted in blue in the fourth quadrant in Fig. 4(d). It contains one single $10\bar{1}1$ reflection parallel to *c*-ScN 113, which is marked by a gray dotted square.

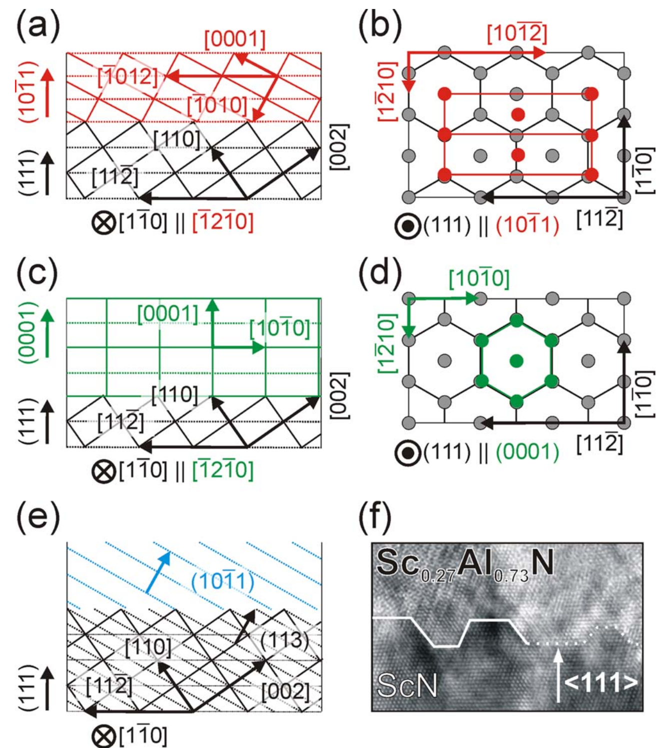

FIG. 5. (Color online) Schematic of the three different epitaxial relationships between rocksalt ScN(111) seed layer (gray) and the wurtzite structured (*w*) film found in Fig. 4(d), with (a), (c), and (e) showing views along the $[1\bar{1}0]$ zone axis, and (b) and (d) showing top views of the 111 ScN surface. (a) and (b) correspond to *w*-$Sc_{1-x}Al_xN(10\bar{1}1)\parallel$ScN(111) (red), (c) and (d) correspond to *w*-$Sc_{1-x}Al_xN(0001)\parallel$ScN(111) (green), and (e) correspond to *w*-$Sc_{1-x}Al_xN(10\bar{1}1)\parallel$ScN(113) (blue). (f) shows a typical high resolution XTEM image of the rough interface between ScN and the film.

The absence of other reflections precludes unique determination of the corresponding crystallite orientations. Other than the possibility that the corresponding zone axis contains only the $10\bar{1}1$ pole, the absence of more reflections could be due to the magnification of the diffraction pattern, which depends on the camera length, resulting in other reflections lying outside the visible area. It is the first time that this crystallographic orientation relationship is observed and it is shown along $[1\bar{1}0]$ of the seed layer in Fig. 5(e). The fact that many different grain orientations are present in the film can be attributed to the rough interface between the seed layer and the $Sc_{0.49}Al_{0.51}N$ film, as shown in a high resolution XTEM image in Fig. 5(f). It contains a large sampling of seed layer surface facet orientations, which allows for nucleation of several different crystallographic orientations of *w*-$Sc_{1-x}Al_xN$.

An XTEM overview image from a sample with $x=0.90$ is shown in Fig. 4(e). The substrate and seed layer are of the same structure as the previous samples. The film appears to be smooth without any strong contrast, which can be due to a nanocrystalline structure or a high amount of defects. The SAED pattern from this sample is shown in Fig. 4(f) and contains contributions from three different grain orientations. The pattern is divided into three sections for clarity but can be completely indexed if the highlighted patterns in each section are extended. The highlighted reflections in the sections show

Downloaded 04 Nov 2009 to 130.236.83.91. Redistribution subject to AIP license or copyright; see http://jap.aip.org/jap/copyright.jsp

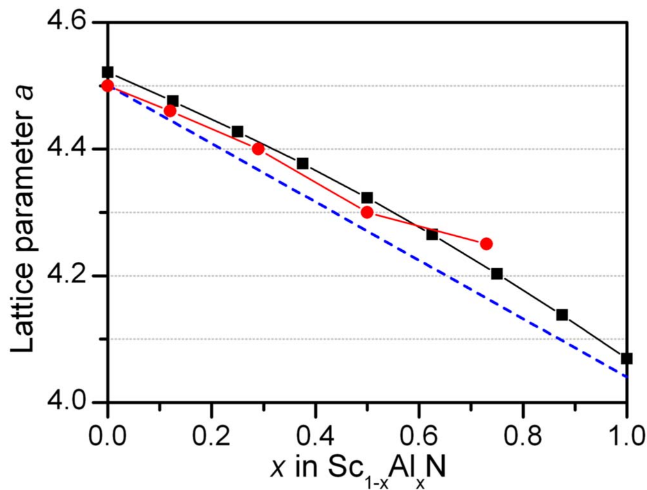

FIG. 6. (Color online) Lattice parameter a vs composition for $Sc_{1-x}Al_xN$ thin films, with x varying from 0 to 1, showing experimental data (red dots), together with calculated values (black squares) replotted from Ref. 24 and Vegard's rule (dashed blue line) drawn as a straight line using experimental lattice parameters from Refs. 25 and 16.

(1) cube-on-cube epitaxial contribution,
(2) growth of film $(10\bar{1}1)\|$ScN(111) and film $[\bar{1}2\bar{1}0]\|$ ScN$[1\bar{1}0]$, and
(3) growth of film (0001)$\|$ScN(111) and film $[\bar{1}2\bar{1}0]\|$ ScN$[1\bar{1}0]$.

This yields a similar pattern as for the sample with $x=0.73$. The only difference is that w-$Sc_{1-x}Al_xN(10\bar{1}1)\|$ c-ScN(113), which was visible in the fourth quadrant in Fig. 4(d), is not present in this sample. The reason why this orientation relationship showed up in a film with lower AlN content, but not in this film, is not understood but could be due to the film growth kinetics.

In Fig. 6 calculations of lattice parameters for a cubic solid solution of $Sc_{1-x}Al_xN$ are replotted from Ref. 24 with black squares. A positive deviation from Vegard's rule[39] (dashed straight line) from experimentally reported values of ScN (Ref. 25) and AlN (Ref. 16) can be seen. Such a small overestimation of the experimental values is common for calculations using the GGA functional and a similar shape of the calculated curve was also observed in lattice parameter calculations for different related systems, such as $Ti_{1-x}Al_xN$, $Cr_{1-x}Al_xN$, and $Hf_{1-x}Al_xN$.[24] The experimental curve (with red dots) in Fig. 6 is a combination of the compositions achieved from RBS and the lattice parameters calculated from XRD data. For film compositions with x up to 0.51, the curve is positioned between the line corresponding to Vegard's rule and the calculated values. In addition, SAED shows exclusively cube-on-cube epitaxy for these films to the ScN(111) seed layers. We therefore conclude that AlN molar fractions of at least 51% can be dissolved into c-ScN, forming a homogeneous cubic solid solution of $Sc_{49}Al_{51}N$. The film with $x=0.73$, which was deposited on an $MgAl_2O_4(111)$ substrate, yielded an XRD peak corresponding to a cubic lattice parameter of 4.25 Å. XRD pole figures from this sample show that it is cube-on-cube epitaxial growth of the film on ScN(111). The film lattice parameter gives a relatively large positive deviation from the calculated values in Fig. 6, in contrast to our expectations and the results for lower AlN contents. From the given lattice parameter and by applying Vegard's rule, the cubic part of the film is expected to consist of $Sc_{0.40}Al_{0.60}N$. In addition, SAED shows three different hexagonal epitaxial relationships to the seed layer, which all originate from phases with lattice parameters equal to w-AlN. These wurtzite structure phases are probably w-AlN or AlN rich w-$Sc_{1-x}Al_xN$ due to the residuals of Al and N for an overall film composition of $Sc_{0.27}Al_{0.73}N$. The results above show that the maximum AlN molar fraction that can be dissolved into ScN is ~60%. For samples with even higher AlN contents, SAED shows similar hexagonal epitaxial relationships of the film to the seed layer. Those films do not exhibit peaks in XRD, which may be due to small, nanometer size, crystallites. Although the structure is expected to be hexagonal, cubic crystallites cannot be excluded due to substrate peak overlaps. Finally, it was seen in XTEM that the film density increases with higher AlN content, which supports the assumption from ERDA that films with more AlN hinder the diffusion of O into the films when exposing them to air.

Mixing enthalpy calculations for c-, w-, and zb-$Sc_{0.50}Al_{0.50}N$ solid solutions were performed. They yield that the mixing enthalpies (H^{mix}) per formula unit (f.u.) are $H^{mix}_{rocksalt}=0.406$ eV/f.u., $H^{mix}_{wurtzite}=0.357$ eV/f.u., and $H^{mix}_{zinc\ blende}=0.488$ eV/f.u., respectively. Due to these rather high positive values of the mixing enthalpies, the solid solution at intermediate concentrations can only be metastable with respect to phase separation at all relevant temperatures. This is confirmed by a mean field analysis, which indicates that temperatures above 8000 K would be needed to stabilize any $Sc_{0.50}Al_{0.50}N$ solid solution by means of configurational entropy. The wurtzite structure is energetically favorable compared to both c and zb structures at an AlN molar fraction of 50%. The fact that we can stabilize AlN molar fractions up to ~60% in the rocksalt solid solution is due to the magnetron sputter process, which operates far from an equilibrium state and known to enable the formation of solid solutions of otherwise immiscible systems.[40] The fact that the rocksalt structure has higher mixing enthalpies than the wurtzite structure for $Sc_{0.50}Al_{0.50}N$ solid solutions underlines the importance of the growth parameters. Use of a ScN seed layer, which acts as a cubic growth template, extends the limits for rocksalt structure growth at the expense of the wurtzite structure.

IV. CONCLUSIONS

Thin films of $Sc_{1-x}Al_xN$ with x varied from 0 to 1 were deposited by reactive MSE, onto MgO(111) substrates with a rocksalt structure (c)-ScN(111) seed layer, from elemental Al and Sc targets at 600 °C. AlN molar fractions of up to ~60% have been dissolved into c-ScN(111) forming a cubic solid solution of $Sc_{1-x}Al_xN$ with $0 \leq x \leq 0.60$. Higher AlN contents result in a phase separation into wurtzite structure (w)-AlN or AlN-rich w-$Sc_{1-x}Al_xN$. These two phases exhibit up to four epitaxial relationships to the ScN(111) seed layer: The cube-on-cube relationship, $Sc_{1-x}Al_xN(0001)\|$ScN(111)

Downloaded 04 Nov 2009 to 130.236.83.91. Redistribution subject to AIP license or copyright; see http://jap.aip.org/jap/copyright.jsp

with $Sc_{1-x}Al_xN[\bar{1}2\bar{1}0] \| ScN[1\bar{1}0]$, $Sc_{1-x}Al_xN(10\bar{1}1) \| ScN(111)$ with $Sc_{1-x}Al_xN[\bar{1}2\bar{1}0] \| ScN[1\bar{1}0]$, and $Sc_{1-x}Al_xN(10\bar{1}1) \| ScN(113)$ of which the two last ones are novel. First-principles density functional theory calculations yield a metastability of *c*-, *w*-, and zb-$Sc_{0.50}Al_{0.50}N$ solid solution with respect to phase separation.

ACKNOWLEDGMENTS

We acknowledge the financial support given by the Swedish Foundation for Strategic Research (SSF) Center on Materials Science for nanoscale Surface Engineering (MS^2E) and the Swedish Research Council (VR). The calculations were performed at the Swedish National Supercomputer Centre (NSC) using resources provided by the Swedish National Infrastructure for Computing (SNIC). We also acknowledge the assistance of Dr. Jens Jensen in making RBS and ERDA measurements at the Tandem Laboratory in Uppsala.

[1]K. Adomi, J.-I. Chyi, S. F. Fang, T. C. Shen, S. Strite, and H. Morkoc, Thin Solid Films **205**, 182 (1991).
[2]T. Seppänen, Ph.D. dissertation No. 1027, Linköping Studies in Science and Technology, 2006.
[3]M. G. Moreno-Armenta, L. Mancera, and N. Takeuchi, Phys. Status Solidi B **238**, 127 (2003).
[4]A. BenFredj, Y. Oussaifi, N. Bouarissa, and M. Said, Phys. Status Solidi B **243**, 2780 (2006).
[5]S. Zerroug, F. Ali Sahraoui, and N. Bouarissa, J. Appl. Phys. **103**, 063510 (2008).
[6]O. Knotek, W. D. Münz, and T. Leyendecker, J. Vac. Sci. Technol. A **5**, 2173 (1987).
[7]K. Kutschej, P. H. Mayrhofer, M. Kathrein, P. Polcik, R. Tessadri, and C. Mitterer, Surf. Coat. Technol. **200**, 2358 (2005).
[8]K. Bobzin, E. Lugscheider, R. Nickel, and P. Immich, Materialwiss. Werkstofftech. **37**, 833 (2006).
[9]C. Höglund, J. Birch, M. Beckers, B. Alling, Zs. Czigány, A. Mücklich, and L. Hultman, Eur. J. Inorg. Chem. **2008**(8), 1193 (2008).
[10]M. Akiyama, T. Kamohara, K. Kano, A. Teshigahara, Y. Takeuchi, and N. Kawahara, Adv. Mater. (Weinheim, Ger.) **21**, 593 (2009).
[11]S. Strite and H. Morkoc, J. Vac. Sci. Technol. B **10**, 1237 (1992).
[12]P. Limsuwan, N. Udomkan, S. Meejoo, and P. Winotai, Int. J. Mod. Phys. B **19**, 2073 (2005).
[13]A. Kumar, H. L. Chan, J. J. Weimer, and L. Sanderson, Thin Solid Films **308-309**, 406 (1997).
[14]G. A. Slack, R. A. Tanzilli, R. O. Pohl, and J. W. Vandersande, J. Phys. Chem. Solids **48**, 641 (1987).
[15]C. F. Cline and J. S. Kahn, J. Electrochem. Soc. **110**, 773 (1963).
[16]H. Vollstädt, E. Ito, M. Akaishi, S. Akimoto, and O. Fukunaga, Proc. Jpn. Acad., Ser. B: Phys. Biol. Sci. **66**, 7 (1990).
[17]Y. C. Cheng, X. L. Wu, J. Zhu, L. L. Xu, S. H. Li, and P. K. Chu, J. Appl. Phys. **103**, 073707 (2008).
[18]D. Gall, I. Petrov, N. Hellgren, L. Hultman, J.-E. Sundgren, and J. E. Greene, J. Appl. Phys. **84**(11), 6034 (1998).
[19]K. A. Gschneider, Jr., G. A. Melson, D. A. Melson, D. H. Youngblood, and H. H. Schock, in *Scandium: Its Occurrence*, edited by C. T. Horovitz (Academic, London, 1975), Vol. 165, cited in Ref. 32.
[20]W. R. L. Lambrecht, Phys. Rev. B **62**, 13538 (2000).
[21]D. Gall, M. Städele, K. Järrendahl, I. Petrov, P. Desjardins, R. T. Haasch, T.-Y. Lee, and J. E. Greene, Phys. Rev. B **63**, 125119 (2001).
[22]C. Stampfl, W. Mannstadt, R. Asahi, and A. J. Freeman, Phys. Rev. B **63**, 155106 (2001).
[23]H. A. Al-Brithen, A. R. Smith, and D. Gall, Phys. Rev. B **70**, 045303 (2004).
[24]B. Alling, A. Karimi, and I. Abrikosov, Surf. Coat. Technol. **203**, 883 (2008).
[25]W. Lengauer, J. Solid State Chem. **76**, 412 (1988).
[26]N. Farrer and L. Bellaiche, Phys. Rev. B **66**, 201203(R) (2002).
[27]D. Gall, I. Petrov, L. D. Madsen, J.-E. Sundgren, and J. E. Greene, J. Vac. Sci. Technol. A **16**, 2411 (1998).
[28]H. A. Al-Brithen and A. R. Smith, Appl. Phys. Lett. **77**, 2485 (2000).
[29]J. P. Dismukes, W. M. Yim, J. J. Tietjen, and R. E. Novak, J. Cryst. Growth **9**, 295 (1971).
[30]M. A. Moram, Z. H. Barber, and C. J. Humphreys, Thin Solid Films **516**, 8569 (2008).
[31]J. Birch, S. Tungasmita, and V. Darakchieva, *Vacuum Science and Technology: Nitrides as Seen by Technology* (Research Signpost, Trivandrum, 2002), pp. 421–456.
[32]M. S. Janson, CONTES conversion of time-energy spectra—a program for ERDA data analysis, Internal Report, Uppsala University, 2004.
[33]P. E. Blöchl, Phys. Rev. B **50**, 17953 (1994).
[34]G. Kresse and J. Hafner, Phys. Rev. B **48**, 13115 (1993).
[35]G. Kresse and J. Hafner, Phys. Rev. B **49**, 14251 (1994).
[36]J. Perdew, K. Burke, and M. Ernzerhof, Phys. Rev. Lett. **77**, 3865 (1996).
[37]A. Zunger, S. H. Wei, L. G. Ferreira, and J. E. Bernard, Phys. Rev. Lett. **65**, 353 (1990).
[38]B. Alling, A. V. Ruban, A. Karimi, O. E. Peil, S. I. Simak, L. Hultman, and I. A. Abrikosov, Phys. Rev. B **75**, 045123 (2007).
[39]L. Vegard, Z. Phys. **5**, 17 (1921).
[40]I. Petrov, P. B. Barna, L. Hultman, and J. E. Greene, J. Vac. Sci. Technol. A **21**, S117 (2003).

Downloaded 04 Nov 2009 to 130.236.83.91. Redistribution subject to AIP license or copyright; see http://jap.aip.org/jap/copyright.jsp